J Mater Sci (2009) 44:5579–5587
DOI 10.1007/s10853-009-3784-1

Structural study of Li_2MnO_3 by electron microscopy

**C. H. Lei · J. G. Wen · M. Sardela · J. Bareño ·
I. Petrov · S.-H. Kang · D. P. Abraham**

Received: 9 April 2009 / Accepted: 28 July 2009 / Published online: 8 August 2009

Abstract Detailed crystallographic data on high-quality Li_2MnO_3 material has been obtained using a combination of X-ray diffraction (XRD), selected-area electron diffraction (SAED), high-resolution electron microscopy (HREM), and 0.1 nm probe high-angle annular dark-field imaging (HAADF) in a scanning transmission electron microscope. A high-purity Li_2MnO_3 powder was annealed at 950 °C for 3 days to obtain predominantly defect-free grains which average size was 3.0 ± 1.5 µm. Rietveld refinement indicated that the *C2/m* spacegroup provided the best fit for the XRD data. Electron diffraction patterns obtained along various zone axes, on defect-free oxide particles, could be uniquely indexed to the monoclinic structure. HREM and HAADF images of defect-free grains were consistent with a Li–Mn–Mn– arrangement, i.e., lithium ordering in the transition metal planes. Low-magnification TEM images occasionally revealed stacking defects within oxide particles. HREM images of sample areas containing defects revealed a low density of stacking faults within the monoclinic sequence, resulting in a trigonal *P3₁12* local arrangement.

Introduction

Material development for alternative energy technologies has accelerated in recent years because of environmental, economic, and national security concerns associated with the use of petroleum and petroleum products. Manganese oxide compounds are of significant interest to the energy industry because they are cheap, plentiful, non-toxic, and environmentally benign [1]. These compounds can be synthesized in numerous crystalline and disordered forms, each with distinctive physical and electrochemical properties. The γ-MnO_2 phase is well known for its application in primary 1.5 V Zn/MnO_2 alkaline cells [2]. Manganese oxide is the electrocatalyst in commercial Zn–air alkaline batteries, which have been widely used for several decades [3]. Amorphous MnO_2 compounds are being actively examined as electrodes for asymmetric electrochemical ultracapacitors as a low-cost alternative to hydrous RuO_2 compounds [4, 5]. Lithium manganese oxides and their proton (exchanged for lithium) variants are of interest as electrocatalysts for oxygen reduction in lithium–air cells [6]. Lithium manganese oxides are especially important as electroactive materials in rechargeable lithium and lithium-ion batteries because of their ability to serve as lithium intercalation hosts [1]. The spinel $LiMn_2O_4$ is being used in commercial lithium-ion cells either on its own or in combination with other lithium-intercalating oxides. Other spinels, such as $Li_4Mn_5O_{12}$, and defect spinels, such as $Li_2Mn_4O_9$, are also known to reversibly intercalate and deintercalate lithium over many cycles [1, 7–10]. The insertion or extraction of lithium from these compounds is based on the ability of Mn to oscillate between various oxidation states. In addition, a partial substitution of manganese with transition metals (TMs) such as Ni, Co, Cr makes it possible to tune the cycling performance and aging behavior of these compounds [11–14].

In contrast to the above-mentioned lithium manganese oxides, Li_2MnO_3 is known to be electrochemically inactive for lithium insertion and extraction, in its microcrystalline

---

C. H. Lei · J. G. Wen · M. Sardela · J. Bareño · I. Petrov
Frederick Seitz Materials Research Laboratory, University
of Illinois, 104 S. Goodwin Avenue, Urbana, IL 61801, USA

S.-H. Kang · D. P. Abraham (✉)
Chemical Sciences and Engineering Division, Argonne National
Laboratory, 9700 South Cass Avenue, Argonne, IL 60439, USA
e-mail: abraham@anl.gov

form [1, 15]. Li_2MnO_3 can be made lithium-active by leaching Li or Li_2O from the structure; these Li-deficient compounds are reported to have high intercalation capacities and good reversibility [1]. Alternatively, when synthesized in a nanocrystalline form Li_2MnO_3 has been shown to yield capacities up to 200 mAh/g, and excellent capacity retention over multiple cycles [16]. Structural studies of Li_2MnO_3 are of fundamental interest because it represents one of the end members of the $Li_{1+\delta}(TM_xMn_{1-x})_{1-\delta}O_2$ family ($x = 0$, $\delta = 1/3$), where TM stands for a transition metal (e.g., Fe, Ni, Cr, Co) or a combination of them (e.g., $Li_{1+\delta}(Ni_xCo_yMn_{1-x-y})_{1-\delta}O_2$) [11, 17–20]. These compounds typically have a layered rhombohedral ($R\bar{3}m$) structure, and are promising positive electrode materials because of their high capacity and thermal stability. Presently there is ongoing debate in the literature on whether these compounds form homogeneous solid solutions [21] or contain ordered or partially disordered Li_2MnO_3 domains intergrown and integrated with the $LiTMO_2$ structure [22, 23]. Thus, a critical aspect of this debate is the intrinsic structure of Li_2MnO_3 (also written as $Li(Li_{1/3}Mn_{2/3})O_2$) on which there are some conflicting reports. The Li_2MnO_3 structure has been reported to be trigonal ($P3_112$) [24] as well as monoclinic, either $C2/m$ [25–27] or $C2/c$ [28]. Meanwhile, $LiMnO_2$ has been reported to have a stable orthorhombic ($Pmmn$) and a metastable rhombohedral ($R\bar{3}m$) structure which is stabilized by TM additions [29–31].

The purpose of this work is to obtain detailed crystallographic data, both in direct and reciprocal space, on high-quality Li_2MnO_3 material in order to complement the structural information in the literature. We perform high-resolution crystallographic characterization using a combination of X-ray diffraction (XRD), selected-area electron diffraction (SAED), high-resolution electron microscopy (HREM), and 0.1 nm probe high-angle annular dark-field imaging (HAADF) in scanning transmission electron microscopy (STEM). A sample preparation protocol resulting in large, defect-free sample areas in combination with the high lateral resolution of our instruments allowed us to determine the monoclinic nature of Li_2MnO_3. Additionally, we present lattice resolution images of sample areas containing stacking faults within the monoclinic sequence that result in a small fraction of trigonal $P3_112$ local environments.

Experimental section

A high-purity Li_2MnO_3 powder obtained from Strem Chemicals was heat-treated at 950 °C for 3 days to enhance oxide crystallinity. Powder XRD patterns of the material were collected on a Siemens D5000 diffractometer (Cu$K\alpha$ radiation) between 10 and 80° 2θ at a scan rate of 0.25° 2θ/min. The commercial software Jade 8.0 was used for analysis of the X-ray pattern and Rietveld refinement of the crystal structure.

The Li_2MnO_3 powder was then mixed with 8 wt% polyvinylidene difluoride (PVdF) binder and coated on to a 30-μm thick Al foil. Transmission electron microscopy (TEM) samples were prepared from this coated foil in several steps: (1) a 3-mm disk was punched out, (2) the disk was then glued on to a Cu ring TEM grid, (3) the Al current collector was then gently removed leaving only the electrode coating on the Cu-ring, (4) the sample was cooled with liquid nitrogen and then subjected to low-angle (12°) Ar-ion milling at 5 kV from both sides followed by 3 kV milling to perforation. This technique produces large, thin areas that contained many oxide particles suitable for TEM examination.

The sample was first examined by SAED along various zone axes, obtained by tilting to large angles in a FEI CM12 TEM operated at 120 kV, in order to construct the reciprocal space maps of the oxide material. Lattice-resolution transmission electron microscopy was carried out at 200 kV with a JEOL 2010LaB6, while HAADF STEM images were acquired using a JEOL 2200FS instrument equipped with a probe aberration corrector (CEOS GmbH, Heidelberg, Germany). The point-to-point resolution of the JEOL 2010LaB6 is 0.22 nm in the TEM mode, while the resolution of the JEOL 2200FS is 0.1 nm in the HAADF mode.

Results

X-ray diffraction

Figure 1a shows an XRD pattern from the Li_2MnO_3 laminate along with expected peak positions and intensities for the $C2/m$, $C2/c$, and $P3_112$ structures. Overall, the spectrum presents sharp and pronounced peaks, indicative of the good crystalline quality of the sample. Diffraction peaks in the $2\theta = 20°$ to $35°$ range, absent in the rhombohedral $R\bar{3}m$ $LiMnO_2$ structure, are characteristic of Li ordering in the TM layers [25]. An expanded spectrum of this area is shown in Fig. 1b. The experimental peaks correspond to the expected position of the $C/2m$ and $P3_112$ structures; additional peaks expected from the $C/2c$ structure at 2θ values of 22.8, 26.2, and 30.3 are absent from the experimental spectrum. In comparison to trigonal $P3_112$, monoclinic $C2/m$ and $C2/c$ spectra are characterized by more numerous diffraction lines in the 2θ angular range above 44°, with notable peak splitting around 44.5° and 65°. Rietveld refinement of the data provides good agreement to both $C2/m$ and $C2/c$ monoclinic Li_2MnO_3 structures, with refinement parameters R of 14.9%, and 16.4%,

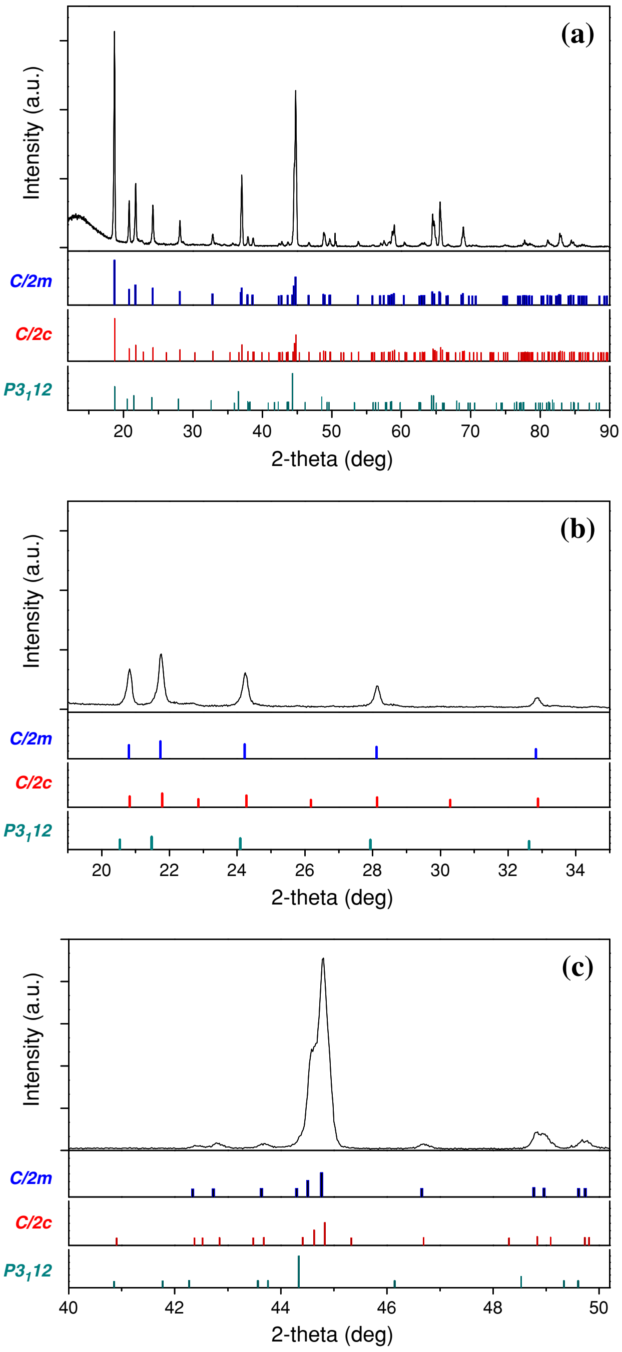

Fig. 1 Experimental X-ray powder diffraction patterns (*top panels*) from the Li_2MnO_3 sample with expected peak positions for *C/2m*, *C/2c*, and $P3_112$ structures: **a** an over-view spectrum, **b** expanded view of the $2\theta = 18$–36° region, and **c** high-resolution display of the region around 44.5° showing a pronounced shoulder in the experimental peak

Table 1 Lattice parameters of the monoclinic unit cell, obtained from Rietveld analysis of the Li_2MnO_3 XRD data

Cell	*a*, nm	*b*, nm	*c*, nm	*β*, °	Volume, nm^3
C2/m	0.4932	0.8535	0.5027	109.41	0.1996

respectively, while the fit to a $P3_112$ structure yielded $R = 42.2\%$. Figure 1c shows an expanded view of the region between 40° and 50° illustrating the pronounced peak splitting in the experimental data in the 2θ region around 44.5° and 47° which is indicative of the monoclinic structure of the sample. Monoclinic lattice parameters resulting from the Rietveld analysis, given in Table 1, are in good agreement with previous reports in the literature [25, 26]. Thus, the XRD data with the Rietveld analysis provide evidence that the well-annealed Li_2MnO_3 material studied here contains predominantly the *C/2m* monoclinic polymorph.

Electron microscopy

Electron microscopy images and diffraction patterns were collected from various oxide particles in the sample. A typical bright field (BF) image of an oxide particle is shown in Fig. 2. Under low magnification BF examination most particles, whose average size was 3.0 ± 1.5 µm, were free of obvious defects; but planar defects were observed locally in a few particles, as seen in Fig. 2. In the following paragraphs, we focus on electron diffraction patterns and lattice resolution images from defect-free regions; defect-containing areas are considered later in the article.

Electron diffraction

Figure 3 provides six typical SAED patterns recorded along different zone axes (indicated in the labels) from defect free areas of different grains. Such patterns were collected on multiple grains by tilting the sample to angles corresponding to the desired zone axis, following Kikuchi

Fig. 2 Low-magnification bright field TEM image of the Li_2MnO_3 sample showing micrometer-size grains with platelet-like defects (see *arrow*) localized in areas of some hundreds of nanometers

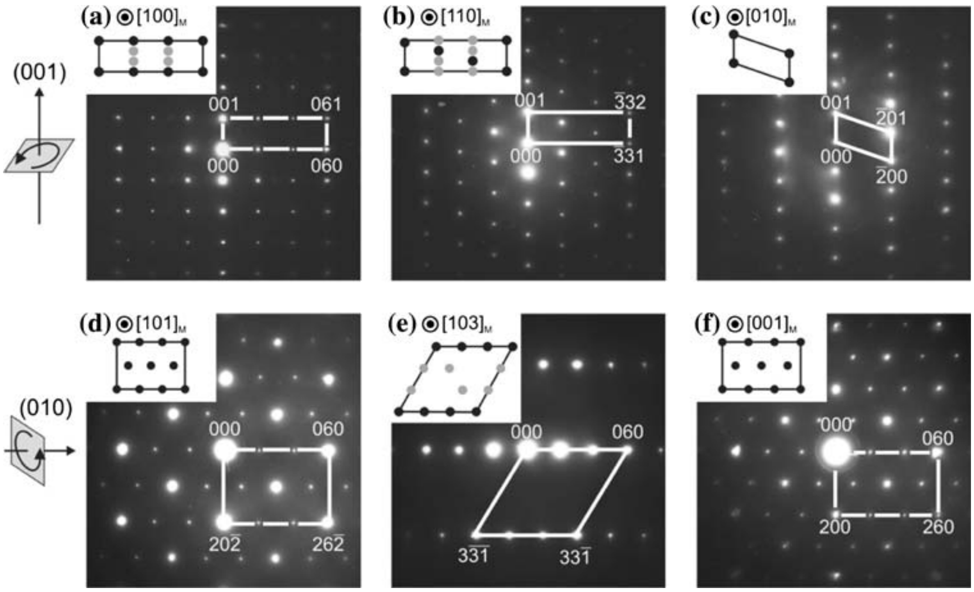

Fig. 3 Six typical selected area electron diffraction (SAED) patterns recorded along different zone axes (indicated in the labels) from defect free areas of different grains. The patterns are indexed with respect to the monoclinic (*C2/m*) unit cell. The reciprocal unit cell corresponding to the rhombohedral $R\bar{3}m$ $LiMnO_2$ structure is outlined on each diffraction pattern with *white lines*. The inset on each panel presents a schematic drawing showing the position of the observed monoclinic reflections (*black dots*) and additional reflections expected from a trigonal ($P3_112$-Li_2MnO_3) structure (*grey dots*)

line maps. The patterns are indexed with respect to the monoclinic *C2/m* unit cell, as indicated by the subindex M in the zone symbols $[uvw]_M$, and the reciprocal unit cell corresponding to the rhombohedral $R\bar{3}m$ $LiMnO_2$ structure is outlined on each diffraction pattern with white lines. The inset on each panel presents a schematic drawing showing the position of the observed monoclinic reflections (black dots) and additional reflections expected from a trigonal $P3_112$ structure (gray dots). Patterns (a) through (c) are recorded along the $[100]_M$, $[110]_M$, and $[010]_M$ zone axes, respectively, corresponding to a rotation of the structure around the (001) pole (normal to the hexagonal metal- and oxygen-planes). Patterns (d) through (f) are recorded along the $[101]_M$, $[103]_M$, and $[001]_M$ zone axes, respectively, corresponding to a rotation of the structure around the (010) pole (parallel to the nearest-neighbor bond direction within hexagonal planes). Patterns (a) and (d) are also related by a rotation around the (010) pole.

Compared to the unit cell expected for rhombohedral $R\bar{3}m$ $LiMnO_2$, the experimental patterns exhibit additional reflections at 1/3 g_{020} positions, due to the 1 × 3 arrangement of Li atoms within $LiMn_2$ planes [24], in agreement with the XRD data. The absence of $P3_112$ exclusive reflections on the experimental patterns (gray dots in the schematic insets) in Fig. 2a, b, and e, is evidence of the overall monoclinic structure of the analyzed Li_2MnO_3 material.

Electron imaging

Figures 4, 5, 6, 7 present HREM, HAADF images of defect-free areas of the sample recorded along the $[100]_M$, $[110]_M$, $[010]_M$, and $[001]_M$ zone axes, respectively, together with structural models of the corresponding projections of the *C2/m* and $P3_112$ Li_2MnO_3 structures. In the following paragraphs, we describe the experimental micrographs, which we discuss and compare to the structural models later in "Discussion" section.

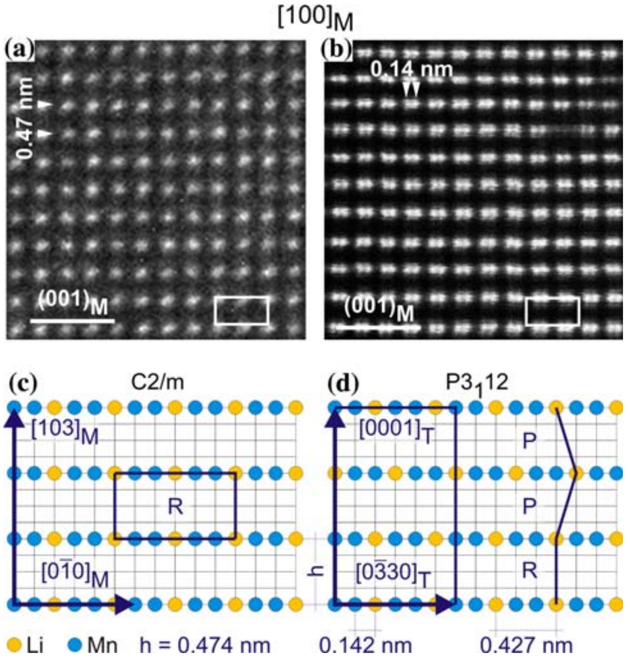

Fig. 4 Experimental **a** HRTEM and **b** HAADF images of a nearly defect-free area of a Li_2MnO_3 sample, recorded along the (monoclinic) $[100]_M$ zone axis. *White boxes* in the bottom-right corner of the panels indicate the projected unit cell of the crystal structure. **c**, **d** Scale drawings of the **c** monoclinic *C2/m* and **d** trigonal $P3_112$ Li_2MnO_3 structures, projected along the $[100]_M$ zone axis. *Yellow* and *blue* dots represent pure Li- and Mn-atomic columns, respectively, in $LiMn_2$ planes; O- and Li-planes have been omitted for clarity. *Dark blue boxes* indicate the projected unit cell of the structure. Plane-stacking sequences resulting in parallelogram- and rectangular-meshes are labeled P and R, respectively

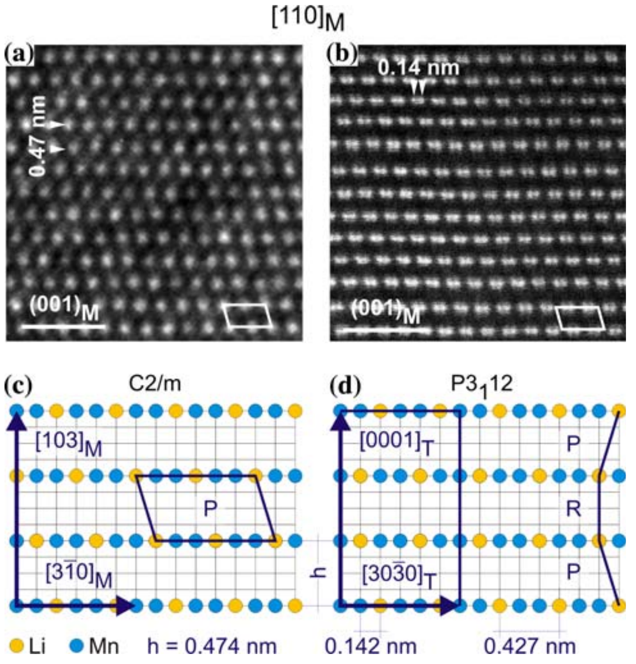

Fig. 5 Experimental **a** HRTEM and **b** HAADF images of a nearly defect-free area of a Li_2MnO_3 sample, recorded along the (monoclinic) $[110]_M$ zone axis. *White boxes* in the bottom-right corner of the panels indicate the projected unit cell of the crystal structure. **c**, **d** Scale drawings of the **c** monoclinic *C2/m* and **d** trigonal *P3₁12* Li_2MnO_3 structures, projected along the $[110]_M$ zone axis. *Yellow* and *blue dots* represent pure Li- and Mn-atomic columns, respectively, in $LiMn_2$ planes; O- and Li- planes have been omitted for clarity. *Dark blue boxes* indicate the projected unit cell of the structure. Plane-stacking sequences resulting in parallelogram- and rectangular-meshes are labeled P and R, respectively

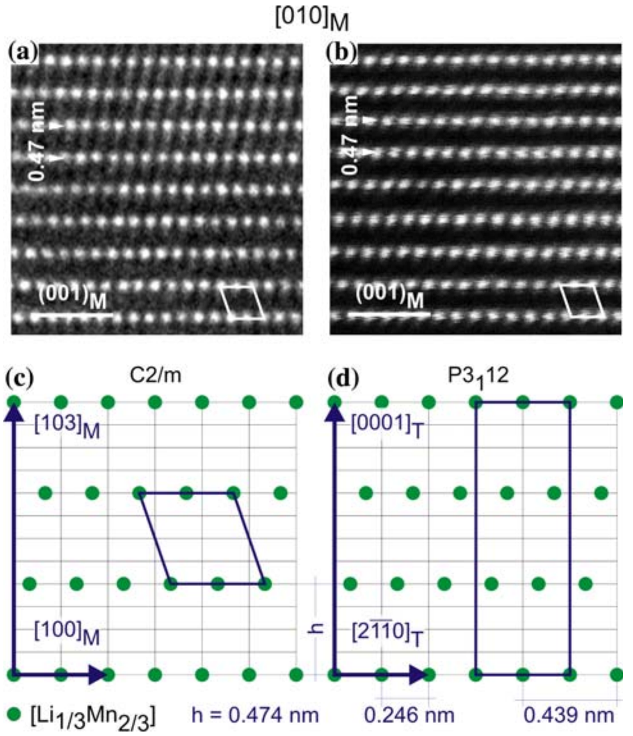

Fig. 6 Experimental **a** HRTEM and **b** HAADF images of a nearly defect-free area of a Li_2MnO_3 sample, recorded along the (monoclinic) $[010]_M$ zone axis. *White boxes* in the bottom-right corner of the panels indicate the projected unit cell of the crystal structure. **c**, **d** Scale drawings of the **c** monoclinic *C2/m* and **d** trigonal *P3₁12* Li_2MnO_3 structures, projected along the $[010]_M$ zone axis. *Green dots* represent atomic columns in $LiMn_2$ planes; O- and Li-planes have been omitted for clarity. *Dark blue boxes* indicate the projected unit cell of the structure

HREM images are formed by recombining the transmitted beam with multiple diffracted beams in a given zone axis. The phase interference between these beams results in a periodic fringe contrast representative of different atomic columns, which allows the unique determination of lattice spacing and symmetries of the sample. HAADF images are formed by collecting electrons scattered by the specimen with a high annular detector (angular range > 50 mrad). In HAADF images, the intensity in each pixel is proportional to the incoherent scattering at each beam position, which in turn is a function of both the average atomic number Z of the projected atomic column and the local specimen thickness. As light elements, Li and O, contribute weakly to electron scattering at higher angles, the HAADF image can be regarded as directly depicting the positions of the Mn-rich columns.

Figures 4 and 5 present the results along the $[100]_M$ and $[110]_M$ zone axes, respectively; i.e., along two equivalent second-nearest neighbor directions (or normal to the bond directions) in the hexagonal planes, with the plane normal running vertical to the figure. Both HREM and HAADF micrographs show a rectangular (R) or parallelogram (P) (Figs. 4 and 5, respectively) pattern of bright spots, consistent with the projection of a monoclinic structure along the Li columns in the Mn-planes [32]. The vertical spacing between two consecutive rows in the images is 0.47 nm in agreement with the 0.474 nm spacing between consecutive $LiMn_2$ planes in Li_2MnO_3. The horizontal overall periodicity of the images is 0.43 nm, corresponding to three times the projected distance between atomic columns ($\delta_{100} = b/6 \approx 0.142$ nm) at hexagonal planes in Li_2MnO_3. Due to the higher resolution in HAADF mode, a single bright dot appearing in the HREM micrographs (Figs. 4a and 5a) is resolved into two separate spots in the HAADF micrographs (Figs. 4b and 5b); these spots are 0.14 nm apart, corresponding to δ_{100}.

Figure 6 presents the results along the $[010]_M$ zone axis; i.e., along the nearest-neighbor (or the bond) direction in the hexagonal planes, with the plane normal running vertical to the figure. Both the HREM and HAADF micrographs (Fig. 6a and b, respectively) show a *P* pattern of bright spots with a characteristic angle of 110°, corresponding to the lattice angle β of *C2/m* Li_2MnO_3. The vertical spacing between two consecutive rows in the images is 0.47 nm, as in Figs. 4 and 5. The horizontal

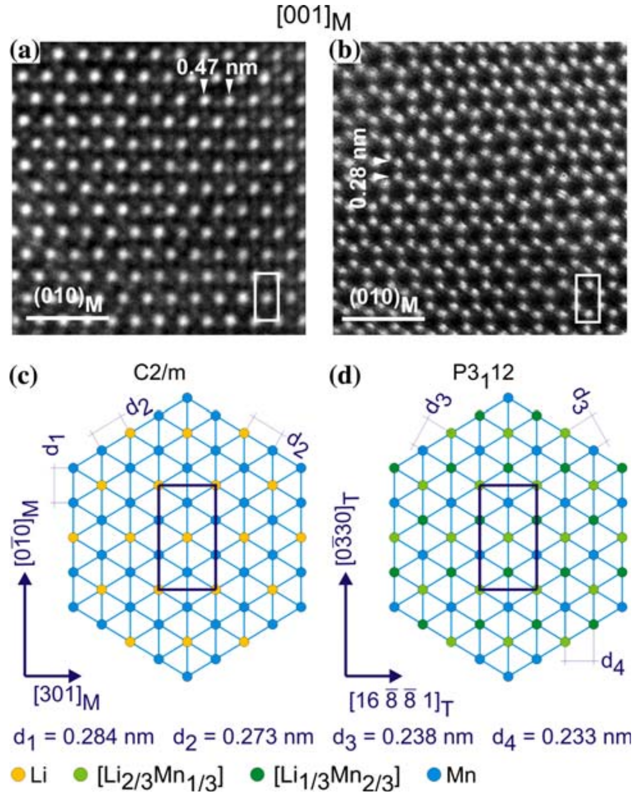

Fig. 7 Experimental **a** HRTEM and **b** HAADF images of a nearly defect-free area of a Li_2MnO_3 sample, recorded along the (monoclinic) $[001]_M$ zone axis. *White boxes* in the bottom-right corner of the panels indicate the projected unit cell of the crystal structure. **c**, **d** Scale drawings of the **c** monoclinic *C2/m* and **d** trigonal *P3₁12* Li_2MnO_3 structures, projected along the $[001]_M$ zone axis. *Colored dots* represent atomic columns in $LiMn_2$ planes (corresponding compositions are given in the legend); O- and Li- planes have been omitted for clarity. Blue boxes indicate the projected unit cell of the structure

periodicity of the images is 0.25 nm, corresponding to the projected distance between atomic columns ($\delta_{010} = a/2 \approx 0.246$ nm) in hexagonal planes in Li_2MnO_3.

Figure 7 presents the results viewed along $[001]_M$ zone axis; i.e., 19° away from normal to $LiMn_2$ (001) planes. The HREM micrograph (Fig. 7a) shows a *quasi*-hexagonal pattern of bright dots corresponding to a projection of the hexagonal $LiMn_2$ planes, which are 19° tilted around the vertical axis of the image, $[010]_M$. The horizontal periodicity of the image is 0.47 nm, corresponding to the projection of the second-nearest neighbor interatomic spacing in the hexagonal planes [$a \cos(19°) \approx 0.466$ nm]. The periodicity along two equivalent *quasi*-hexagonal axes, rotated 120° with respect to the horizontal axis, is 0.49 nm. The corresponding HAADF micrograph (Fig. 7b) also shows a *quasi*-hexagonal pattern of similar periodicity. This time, the repeat motif consists of a hollow hexagonal ring of sharp spots (i.e., a honeycomb pattern). The spot spacing, measured along the undistorted $[010]_M$ direction (vertical axis of the image), is 0.28 nm, corresponding to the nearest-neighbor distance within the hexagonal planes in Li_2MnO_3 ($b/3 \approx 0.284$ nm).

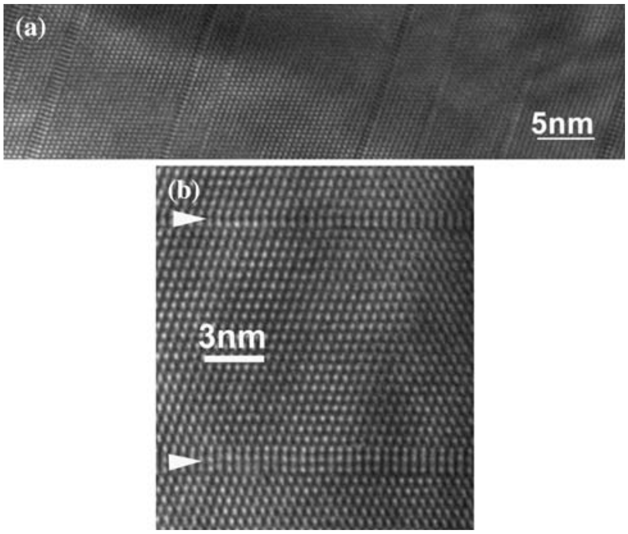

Fig. 8 **a** HREM images showing TM-plane stacking and stacking defects within the Li_2MnO_3 structure. **b** Higher-magnification view showing the presence of rectangular-meshes (R-type stacking) among the parallelogram-mesh (P-type stacking) matrix. Both images are projected along the $[110]_M$ zone axis, the same as in Fig. 5a

Figure 8 presents a typical HREM image of an area of the sample containing stacking faults, such as the planar defects visible in Fig. 2. The image is projected along the $[110]_M$ zone axis, the same as in Fig. 6a. Stacking faults along the plane normal to the hexagonal closed packed TM planes are present within the basic monoclinic matrix. While most of the material shows the P-type pattern typical for the monoclinic structure in this projection, there are R-type stacking meshes extending over only a few atomic distances.

Discussion

Three different Li_2MnO_3 structures have been reported in the literature, one trigonal (*P3₁12*) and two monoclinic (*C2/m* and *C2/c*). All these structures can be derived (upon Li substitution for Mn) from the rhombohedral $R\bar{3}m$ $LiMnO_2$ structure, which, in turn, is structurally related to the (face centered cubic) B1-NaCl structure. In $R\bar{3}m$ $LiMnO_2$, O occupies B1-NaCl anion positions, while Li and Mn alternately occupy the hexagonal close-packed cation planes as illustrated in Fig. 9a. The resulting $R\bar{3}m$ $LiMnO_2$ structure can be viewed as an ABC-stack of hexagonal planes along one of four equivalent B1-NaCl<111> directions, following a –Li–O–Mn–O– sequence. Consequently, the 4-fold symmetry of B1-NaCl structure disappears, and the plane-stacking direction becomes the *c*-axis of the rhombohedral

$R\bar{3}m$ cell, $[0001]_R$. Furthermore, substituting Li for Mn at 1/3 of the atomic positions at Mn-planes (thus becoming $LiMn_2$ planes), results in Li_2MnO_3 (Fig. 9a).

In order to facilitate the comparison between the trigonal and monoclinic variants of Li_2MnO_3, we define a set of crystallographic directions relative to the atomic arrangements in the hexagonal close-packed planes, independently of the specific unit cell choice. Figure 9b shows the characteristic "flower-pattern" arrangement of Li atoms in a $LiMn_2$-plane of Li_2MnO_3 [33, 34]. As indicated on the figure, we define three equivalent A1 directions along second-nearest neighbor directions (i.e., between Li-atoms or normal to bonds) and another three equivalent A2 directions along nearest-neighbor directions (i.e., between Mn atoms or along the bonds) within the plane. The angle between consecutive directions in the A1 or A2 sets is 120°, while both sets are rotated by 30° with respect to each other. We denote the direction normal to the hexagonal closed packed cation plane as A3, while A4 is defined as the direction between two equivalent atomic positions in consecutive $LiMn_2$ planes. Miller indices of crystallographic directions parallel to A1, A2, A3, and A4 in B1-NaCl, $LiMnO_2$, and Li_2MnO_3 structures are presented in Table 2.

Trigonal and monoclinic Li_2MnO_3 differ only in the relative positioning of Li-sublattices between successive $LiMn_2$ planes, which in both cases keep the fcc-like ABC-stacking sequence [25]. As indicated in Fig. 9b, the Li atom of the next $LiMn_2$ layer could occupy one of six equivalent positions B, marked with red stars, relative to a position A of the Li atom at the center of the figure. The top view of two successive $LiMn_2$ layers, namely AB, is shown in Fig. 9c. For the third successive layer, there are two non-equivalent positions that can be occupied by the Li atom while following the ABC stacking of the parent NaCl structure: (1) the Li atom can occupy position C, aligned with the corresponding Li atoms in the A and B layers, forming pure Li $(010)_M$ planes as indicated in Fig. 9d; and (2) the Li atom can occupy position C′, resulting in a 3-fold screw axis normal to the $LiMn_2$ planes as shown in Fig. 9e. The ABC′ stacking of $LiMn_2$ layers results in a trigonal $P3_112$ structure, while ABC stacking results in a monoclinic *C2/m* structure with the *c*-axis of the unit cell joining two consecutive Li atoms in the ABC sequence.

The *a* and *b* unit cell vectors for *C/2m* and $P3_112$ structures are shown in Fig. 9d, e, respectively. For *C2/m* Li_2MnO_3, the *a* axis is along the A1 direction in Fig. 9b; the *b* axis is perpendicular to *a* axis. The *c* axis, $[001]_M$, coincides with the A4 direction (see Fig. 9a) that connects Li atoms of successive $LiMn_2$ layers. The *c*-axis of the trigonal $P3_112$ unit cell, $[0001]_T$, is normal to the $LiMn_2$ planes; while their a- and b-axes are parallel to A1 and A2, respectively. The $P3_112$ structure presents 3-fold rotation symmetry around $[0001]_T$; the lack of such symmetry in

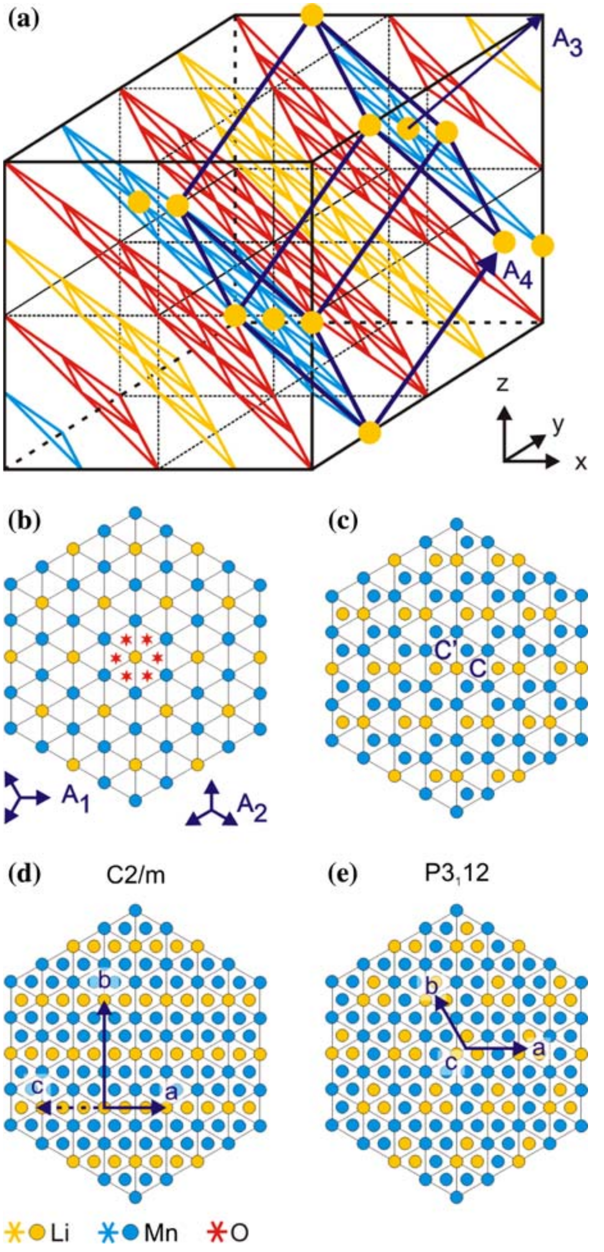

Fig. 9 **a** Schematic of the *C2/m* Li_2MnO_3 structure showing the ABC-stacking sequence of hexagonal Li, O, and $LiMn_2$ planes; as well as the relation between the cubic (*black*) and monoclinic (*dark blue*) unit cells. Atomic positions are indicated by colored line crossings and dots (the color code is given in the legend). **b** Top-view of a $LiMn_2$ plane. Red stars indicate the six equivalent positions for Li in the next $LiMn_2$ plane in the stack. **c** Top-view of two stacked $LiMn_2$ planes. Two non-equivalent positions for Li in the next $LiMn_2$ plane are labeled C and C′. **d** Top-view of a *C2/m* $LiMn_2$ plane stacking sequence, corresponding to site C in panel c. **e** Top-view of a $P3_112$ $LiMn_2$ plane stacking sequence, corresponding to site C′ in panel c. *Blue arrows* in various panels indicate A_1, A_2, A_3, and A_4 crystal directions (see text for details), as well as the **a** and **b** unit vectors of the *C2/m* (panel d) and $P3_112$ (panel e) structures. A discontinuous blue arrow in panel d indicates the direction of the *c*-axis of the *C2/m* structure, projected onto the plane of the figure

Table 2 Relationship between crystallographic directions in B1-NaCl, rhombohedral-$LiMnO_2$ ($R\bar{3}m$), trigonal-Li_2MnO_3 ($P3_112$), and monoclinic-Li_2MnO_3 ($C2/m$) structures

	A1: Normal to bonds in hexagonal planes	A2: Along bonds in hexagonal planes	A3: Normal to hexagonal planes	A4: Along Li-channels
Cubic (B1-NaCl)	$[11\bar{2}]_C$	$[1\bar{1}0]_C$	$[111]_C$	$[112]_C$
Rhombohedral ($R\bar{3}m$)	$[1\bar{1}00]_R$	$[11\bar{2}0]_R$	$[0001]_R$	$[\bar{1}101]_R$
Trigonal ($P3_112$)	$[2\bar{1}\bar{1}0]_T$	$[01\bar{1}0]_T$	$[0001]_T$	$[\bar{2}113]_T$
Monoclinic ($C2/m$)	$[100]_M$	$[010]_M$	$[103]_M$	$[001]_M$

the *C2/m* structure is one key factor that distinguishes between trigonal and monoclinic Li_2MnO_3. The other monoclinic structure (*C2/c*) also follows the ABC stacking sequence [25]. The *C2/c* Li_2MnO_3 unit cell can be thought of as two *C2/m* unit cells stacked along the *c* axis. By convention, the *a*- and *b*-axes of the *C2/c* cell are chosen to point in the opposite direction than their *C2/m* counterparts, and the *c* axis of the *C2/c* cell is chosen along the *ac*-face diagonal of the *C2/m* cell. In addition to the definition of the unit cell, minor relaxations from the ideal atomic positions derived from the $R\bar{3}m$-$LiMnO_2$ structure transform the (010)-mirror planes in the *C2/m* structure into glide planes in the *C2/c* structure.

When viewed along A1 axes, the $LiMn_2$ planes appear as a repeating sequence of two Mn-atomic columns and one Li-column (see Fig. 9b) and the expected intercolumnar distance is $b/6 = 0.142$ nm. The relative in-plane projected displacement between Li-columns in successive $LiMn_2$ planes is indicative of the trigonal or monoclinic stacking sequence. Figures 4d and 5d show two projections of trigonal Li_2MnO_3 along equivalent A1 axes. In this structure, A3 (the vertical axis of the figure) is a 3-fold screw axis, and the structure appears as a zigzagging stack alternating R and P patterns, which is expected to be invariant with respect to the actual choice of projection axis between the three equivalent $\langle 2\bar{1}\bar{1}0\rangle_T$ directions. However, A3 is a 2-fold rotation axis in monoclinic Li_2MnO_3: thus, A1 directions are not crystallographically equivalent and two distinct structure projections are possible. When projected along the $[100]_M$ zone axis, the structure shows the homogeneous (rectangular) R $LiMn_2$ stacking pattern depicted in Fig. 4c and observed experimentally in Fig. 4a (HREM) and b (HAADF). When projected along the $[110]_M$ zone axis, on the other hand, the structure shows the homogeneous (parallelogram) P $LiMn_2$ stacking pattern depicted in Fig. 5c and observed experimentally in Fig. 5a, b.

The overall symmetry of these projections is also revealed in the SAED patterns presented in Fig. 3a, b. The $[100]_M$ SAED pattern in Fig. 3a shows rectangular symmetry, corresponding to the R patterns in Fig. 4a–c; while the $[110]_M$ SAED pattern in Fig. 3b shows oblique symmetry corresponding to the P patterns of Fig. 5a–c. In contrast, all A1 zone axes in trigonal Li_2MnO_3 are equivalent, resulting in similar structure projections and SAED patterns along them. The schematic insets in Fig. 3a, b show that the additional reflections expected from trigonal Li_2MnO_3 (gray dots) results in the same SAED pattern in both cases.

Figure 6c, d shows A2 projections of the monoclinic and trigonal Li_2MnO_3 structures, respectively. Contrary to A1 zone axis projections, A2 zone axes projections cannot distinguish between monoclinic and trigonal Li_2MnO_3. In this case, $LiMn_2$ planes project as rows of equivalent atomic columns, with $LiMn_2$ composition and intercolumnar distance $a/2 \approx 0.247$ nm. The stacking of $LiMn_2$ planes along A3 (vertical axis of the picture) results in a P-type projected structure, with sides parallel to A1 and A4, as can be seen experimentally on Fig. 6a (HREM) and b (HAADF). The corresponding SAED pattern on Fig. 3c shows the expected 2-fold P pattern and, as can be seen in the inset, no additional reflections are expected for a trigonal structure.

The SAED data along A3 (Fig. 3e) displays the 2-fold rotation symmetry of monoclinic Li_2MnO_3; while the additional reflections expected for trigonal Li_2MnO_3 (gray dots in the inset) would result in a 6-fold symmetric pattern, arising from a combination of the trigonal 3-fold screw axis in the structure and the additional centro-symmetry of the pattern due to kinematic diffraction conditions.

Figure 7c, d shows two projections of the monoclinic and trigonal Li_2MnO_3 structures, respectively, along A4; i.e., along Li-channels. The projected monoclinic structure presents a *quasi*-hexagonal pattern, consisting of pure Li- and Mn-atomic columns, with each Li-column surrounded by six Mn-columns in a honeycomb structure. The projected trigonal structure, on the other hand, displays a 2-fold symmetric structure composed of alternating rows of Mn-, $LiMn_2$-, and Li_2Mn-atomic columns. The *quasi*-6-fold symmetry of the corresponding HREM (Fig. 7a) and HAADF (Fig. 7b) images, as well as of the SAED pattern, confirms the monoclinic structure of the sample; while the contrast of the HAADF micrograph is in perfect agreement with the interpretation of low-Z (Li) columns surrounded by six high-Z (Mn) columns.

In summary, a combination of Rietveld refinement of XRD patterns, SAED, HREM, and HAADF analysis of high-quality Li_2MnO_3 powder confirms that defect-free areas of the sample, which can be as big as a few microns, present monoclinic structure. Defects within this structure, such as the area presented in Fig. 8, consist of small (between 1 and 5 $LiMn_2$-plane spacings wide) R-type inclusions within a P-type matrix; which can be regarded as a stack of monoclinic Li_2MnO_3 slabs (P-type matrix) some of which (R-type inclusions) are rotated around the common A3 axis by 60°. Additionally, trigonal Li_2MnO_3 can also be regarded as a faulted stack of monoclinic Li_2MnO_3, where every slab (one *C2/m* unit cell high) is rotated around the common A3 axis by 60°. Such a fault does not require a change of composition and keeps the overall fcc-like plane stacking sequence, affecting only the high-order bonds between atoms in $LiMn_2$ planes; and can be expected to possess very low formation energy. Indeed, previous DFT calculations of Li_2MnO_3 ground-state energy [25] found negligible ($\approx$2 meV/f.u.) differences between the monoclinic and trigonal structures indicating that either the sequence-fault formation energy is very low or that there is a strong interaction between sequencing faults that greatly favors the $P3_112$ arrangement. Li_2MnO_3 alloying with additional TM to form $Li_{1+x}TM_yMn_{1-x-y}O_2$ results in further reduction of the sequence-fault and other defect formation energies as suggested by available experimental reports of, for example, a *quasi*-random stacking sequence in $Li_{1.2}Ni_{0.2}Mn_{0.6}O_2$ [32], monoclinic inclusions within a $P3_112$ matrix in $LiNi_{0.5}Mn_{0.5}O_2$ [24], and the appearance of cubic rock salt structure Fe-rich nanodomains in $Li_{1.2}Mn_{0.4}Fe_{0.4}O_2$ [18].

Summary

The crystal structure of high-purity Li_2MnO_3 samples was examined by XRD and electron microscopy. Rietveld refinement indicated that the *C2/m* spacegroup provided the best fit for the XRD data. Electron diffraction patterns obtained along various zone axes, on defect-free oxide particles, could be uniquely indexed to the monoclinic structure. HREM and HAADF images of defect-free grains were consistent with a Li–Mn–Mn– arrangement, i.e., lithium ordering in the TM planes. Low-magnification TEM images occasionally revealed stacking defects within oxide particles. These planar defects induced a part of $P3_112$ Li_2MnO_3 locally within the parent *C2/m* structure.

Acknowledgements We acknowledge D. Howell at the U.S. Department of Energy (DOE), Office of Vehicle Technologies, for supporting this research. We acknowledge the use of the Center for Microanalysis of Materials (CMM) at the Frederick Sietz Materials Research Laboratory, University of Illinois at Urbana-Champaign (UIUC), which is partially supported by the U.S. Department of Energy under grant DEFG02-91ER45439. Argonne National Laboratory is a U.S. Department of Energy Office of Science laboratory operated by UChicago Argonne LLC under contract DE-AC02-06CH11357.

References

1. Thackeray MM (1997) Progr Solid State Chem 25:1
2. Linden D (ed) (1995) Handbook of batteries. McGraw-Hill, New York
3. Kinoshita K (ed) (1992) Electrochemical oxygen technology. Wiley, New York
4. Lee HY, Goodenough JB (1999) J Solid State Chem 144:220
5. Ghaemi M, Ataherian F, Zolfaghari A, Jafari SM (2008) Electrochim Acta 53:4607
6. Ngala JK, Alia S, Dobley A, Crisostomo VMB, Suib SL (2007) Chem Mater 19:229
7. Tarascon JM, Guyomard D (1993) Electrochim Acta 38:1221
8. Kim J, Manthiram A (1998) J Electrochem Soc 145:L53
9. Julien CM, Massot M, Zaghib K (2004) J Power Sour 136:72
10. Strobel P, Palos AI, Anne M (2001) J Power Sour 97–8:381
11. Balasubramanian M, McBreen J, Davidson IJ, Whitfield PS, Kargina I (2002) J Electrochem Soc 149:A176
12. Ammundsen B, Paulsen J (2001) Adv Mater 13:943
13. Yabuuchi N, Ohzuku T (2003) J Power Sour 119:171
14. Makimura Y, Ohzuku T (2003) J Power Sour 119:156
15. Robertson AD, Bruce PG (2003) Chem Mater 15:1984
16. Jain GR, Yang JS, Balasubramanian M, Xu JJ (2005) Chem Mater 17:3850
17. Thackeray MM, Kang SH, Johnson CS, Vaughey JT, Benedek R, Hackney SA (2007) J Mater Chem 17:3112
18. Kikkawa J, Akita T, Tabuchi M, Shikano M, Tatsumi K, Kohyama M (2008) J Appl Phys 103:104911
19. Weill F, Tran N, Croguennec L, Delmas C (2007) J Power Sour 172:893
20. Pan CJ, Lee YJ, Ammundsen B, Grey CP (2002) Chem Mater 14:2289
21. Lu ZH, Chen ZH, Dahn JR (2003) Chem Mater 15:3214
22. Johnson CS, Li NC, Lefief C, Vaughey JT, Thackeray MM (2008) Chem Mater 20:6095
23. Thackeray MM, Kang SH, Johnson CS, Vaughey JT, Hackney SA (2006) Electrochem Commun 8:1531
24. Meng YS, Ceder G, Grey CP, Yoon WS, Jiang M, Breger J, Shao-Horn Y (2005) Chem Mater 17:2386
25. Breger J, Jiang M, Dupre N, Meng YS, Shao-Horn Y, Ceder G, Grey CP (2005) J Solid State Chem 178:2575
26. Massarotti V, Bini M, Capsoni D, Altomare A, Moliterni AGG (1997) J Appl Crystallogr 30:123
27. Strobel P, Lambertandron B (1988) J Solid State Chem 75:90
28. Riou A, Lecerf A, Gerault Y, Cudennec Y (1992) Mater Res Bull 27:269
29. Ammundsen B, Desilvestro J, Groutso T, Hassell D, Metson JB, Regan E, Steiner R, Pickering PJ (2000) J Electrochem Soc 147:4078
30. Jang YI, Huang BY, Chiang YM, Sadoway DR (1998) Electrochem Solid State Lett 1:13
31. Nath Shukla N, Prasad R (2006) J Phys Chem Solids 67:1731
32. Lei CH, Bareno J, Wen JG, Petrov I, Kang SH, Abraham DP (2008) J Power Sour 178:422
33. Van der Ven A, Ceder G (2004) Electrochem Commun 6:1045
34. Breger J, Meng YS, Hinuma Y, Kumar S, Kang K, Shao-Horn Y, Ceder G, Grey CP (2006) Chem Mater 18:4768